Geophysical Journal International

Geophys. J. Int. (2014) doi: 10.1093/gji/ggu048

Geophysical Journal International Advance Access published March 4, 2014

Post-seismic viscoelastic deformation and stress transfer after the 1960 *M*9.5 Valdivia, Chile earthquake: effects on the 2010 *M*8.8 Maule, Chile earthquake

Min Ding[1] and Jian Lin[2,3]

[1] *Massachusetts Institute of Technology/Woods Hole Oceanographic Institution Joint Program, Woods Hole, MA* 02543, *USA*
[2] *Department of Geology and Geophysics, Woods Hole Oceanographic Institution, Woods Hole, MA* 02543, *USA. E-mail: jlin@whoi.edu*
[3] *College of Ocean and Earth Science, Tongji University, Shanghai* 200092, *China*

Accepted 2014 February 5. Received 2014 February 4; in original form 2013 July 10

SUMMARY

After the 1960 *M*9.5 Valdivia, Chile earthquake, three types of geodetic observations were made during four time periods at nearby locations. These post-seismic observations were previously explained by post-seismic afterslip on the downdip extension of the 1960 rupture plane. In this study, we demonstrate that the post-seismic observations can be explained alternatively by volumetric viscoelastic relaxation of the asthenosphere mantle. In searching for the best-fitting viscosity model, we invert for two variables, the thickness of the elastic lithosphere, H_e, and the effective Maxwell decay time of the asthenosphere mantle, T_M, assuming a 100-km-thick asthenosphere mantle. The best solutions to fit the observations in four sequential time periods, 1960–1964, 1960–1968, 1965–1973 and 1980–2010, each yield a similar H_e value of about 65 km but significantly increasing T_M values of 0.7, 6, 10 and 80 yr, respectively. We calculate the corresponding viscoelastic Coulomb stress increase since 1960 on the future rupture plane of the 2010 *M*8.8 Maule, Chile earthquake. The calculated viscoelastic stress increase on the 2010 rupture plane varies gradually from 13.1 bars at the southern end to 0.1 bars at the northern end. In contrast, the stress increase caused by an afterslip model has a similar spatial distribution but slightly smaller values of 0.1–3.2 bars on the 2010 rupture plane.

Key words: Seismic cycle; Transient deformation; Seismicity and tectonics; Subduction zone processes; Dynamics: seismotectonics; South America.

1 INTRODUCTION

Post-seismic deformation is frequently observed following large earthquakes, which might be associated with post-seismic afterslip and/or volumetric viscoelasic relaxation (Freed 2005; Wang 2007). However, the relative importance of the different mechanisms is still an open issue, mainly because the spatial and temporal coverage of the post-seismic deformation observations is very limited. The world's largest earthquake ever recorded, the 1960 *M*9.5 Valdivia, Chile earthquake, provides a unique opportunity to investigate the post-seismic deformation and the processes that contribute to the deformation.

This study uses three types of geodetic observations collected after the 1960 Chile earthquake near the rupture zone (Fig. 1). Type 1 observations are land-level changes during 1957–1964 along a leveling line in the Central Valley (triangles in Fig. 1; Plafker & Savage 1970). Type 2 observations are land-level changes during 1960–1968 at 155 survey sites along the Chilean coastline and Corcovado Gulf (dots in Fig. 1; Plafker & Savage 1970). Type 3 observations are tidal records at Puerto Montt, which is only available within two time periods, 1965–1973 (Fig. 6a) and 1980–2010 (Fig. 6b), on the Corcovado Gulf coast.

Barrientos & Ward (1990) solved for a slip model that explains the Types 1 and 2 observations. Their inverted slip patches concentrate at two depth ranges, 0–50 km (solid lines in Fig. 1) and 70–150 km (dashed lines in Fig. 1). Co-seismic slip is thought to occur only within the seismogenic zone, whose lower bound has been estimated to be in the range of 48–53 km for the Chilean region (Tichelaar & Ruff 1991). Barrientos & Ward (1990) thus suggested that the upper patches (0–50 km) correspond to co-seismic slip, while the deeper patches (70–150 km) are associated with post-seismic 'afterslip'. In this way, Barrientos & Ward (1990) proposed an afterslip model, that is the deeper patches of their slip model (70–150 km), to explain the post-seismic signals in Types 1 and 2 observations. For Type 3 observations, Barrientos *et al.* (1992) inverted for another afterslip model at the depth of 50–100 km.

In this study, we show that volumetric viscoelastic relaxation of the asthenosphere mantle, as opposed to the post-seismic afterslip models (Barrientos & Ward 1990; Barrientos *et al.* 1992), can explain the Types 1, 2 and 3 geodetic observations equally

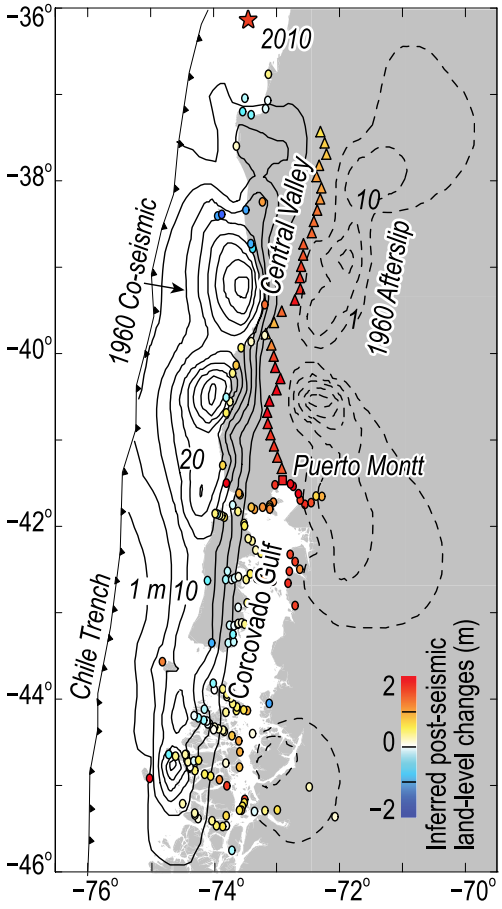

Figure 1. Locations of three types of post-1960 observations: Circles: Type 1; triangles: Type 2 and square: Type 3 data. Also shown are co-seismic (solid contours) and post-seismic afterslip (dashed contours) models of the 1960 Valdivia, Chile earthquake (Barrientos & Ward 1990). The epicentre of the 2010 Maule, Chile earthquake is marked by a red star. The colours of Types 1 and 2 sites indicate the values of inferred post-seismic land-level changes within the corresponding observation time periods.

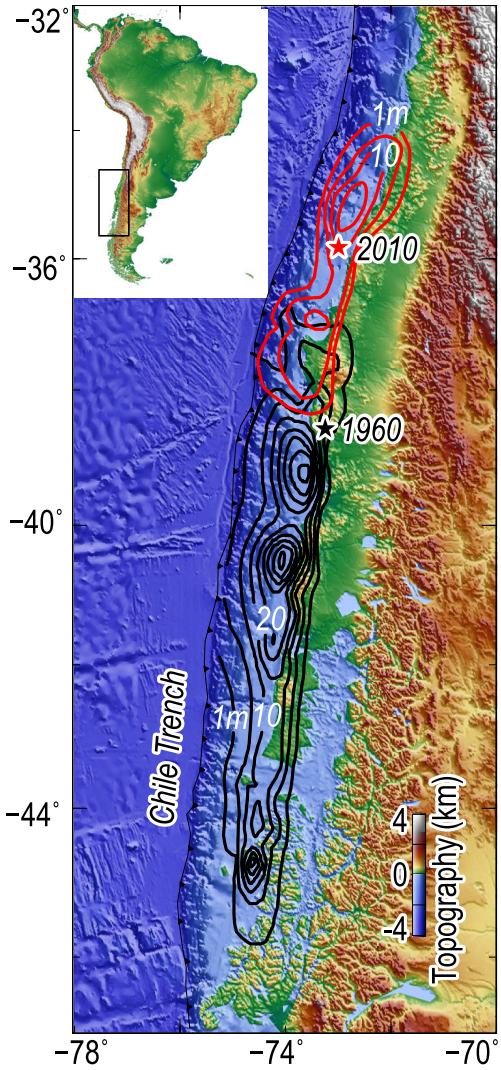

Figure 2. Map-view contours showing slip distributions of the 1960 (black) and 2010 (red) earthquakes, as well as epicentres (stars). Background is land topography and seafloor bathymetry.

well. We first invert for a viscosity model that can best explain the post-seismic deformation data. We then calculate the corresponding viscoelastic stress transfer onto the future rupture plane of the 2010 Maule earthquake (Fig. 2), as well as stress changes associated with an afterslip model.

2 POST-1960 VISCOELASTIC DEFORMATION

2.1 Post-1960 observations

The Type 1 and 2 observations include both co-seismic and post-seismic components. We derive the post-seismic deformation by subtracting co-seismic deformation from the total observations. The co-seismic deformation is calculated as that caused by the co-seismic slip model of Barrientos & Ward (1990) (upper patches, 0–50 km) using the Coulomb 3.3 software (Retrieved on 4 October 2010 from http://earthquake.usgs.gov/research/modeling/coulomb/; Lin & Stein 2004; Toda *et al.* 2005). We then assume that the remaining signals in the Type 1 and 2 data are caused by volumetric viscoelastic relaxation after the 1960 earthquake. The regions of inferred positive post-seismic deformation are located about 100–300 km away from the Chile trench axis (Fig. 4b), in the Central Valley for the Type 1 sites and Corcovado Gulf for the Type 2 sites (Fig. 1). Because the Type 1 and 2 observations were obtained in 1957–1964 and 1960–1968 (Plafker & Savage 1970), we interpret the inferred post-seismic deformation to occur within 1960–1964 and 1960–1968, respectively.

For Type 3 observations, we use the tidal records at the Puerto Montt station in the time periods of 1965–1973 and 1980–1988 from Barrientos *et al.* (1992) as well as 1988–2010 from the PSMSL website (Retrieved on 26 June 2010 from http://www.psmsl.org/data/obtaining). Linear regression yields uplift rates of 4.5 cm yr^{-1} in 1965–1973 (Period a; Fig. 6a) and 0.8 cm yr^{-1} in 1980–2010 (Period b; Fig. 6b).

2.2 Model set-up

We calculate the volumetric viscoelastic deformation on a layered spherical Earth using the VISCO1D code of Pollitz (1992) (Retrieved 23 December 2010 from http://earthquake.usgs.gov/research/software/#VISCO1D). In this code, a co-seismic slip model and a series of Earth viscosity models are specified. The co-seismic slip model is assumed to be the same as the upper slip

Table 1. Parameters for post-1960 viscoelastic relaxation models.

Parameters	Description	Value
H_e	Thickness of the elastic lithosphere (km)	50–80
ρ_e	Range of the density of the elastic lithosphere (kg m^{-3})	2.6–3.38 $\times$ 10^3
λ_e	Range of the Lamé's first parameter of the elastic lithosphere (Pa)	2.93–7.86 $\times$ 10^{10}
μ_e	Range of the shear modulus of the elastic lithosphere (Pa)	2.49–6.82$\times$10^{10}
η_e	Viscosity of the elastic lithosphere (Pa·s)	1 $\times$ 10^{29}
H_a	Thickness of the asthenosphere mantle (km)	100
ρ_a	Range of the density of the asthenosphere mantle (kg m^{-3})	3.38–3.44 $\times$ 10^3
λ_a	Lamé's first parameter of the asthenosphere mantle (Pa)	7.86 $\times$ 10^{10}
μ_a	Shear modulus of the asthenosphere mantle (Pa)	6.70 $\times$ 10^{10}
η_a	Viscosity of the asthenosphere mantle (Pa·s)	1 $\times$ 10^{18}–2 $\times$ 10^{21}
T_M	Effective Maxwell decay time of the asthenosphere mantle defined as $2\eta_a/\mu_a$ (yr)	0.31–640
η_{lower}	Viscosity of the lower mantle (Pa·s)	1 $\times$ 10^{22}
s	Co-seismic slip of the 1960 rupture (m)	0–40 m
θ	Strike of the 1960 fault plane	7°
δ	Dip of the 1960 slip model	20°
λ	Rake of the 1960 slip model	105°
H_s	Maximum depth of the co-seismic slip plane (km)	60

patches of Barrientos & Ward (1990) for the 1960 earthquake (solid contours in Fig. 1). We define a three-layered Earth viscosity model that includes a low-viscosity asthenosphere mantle layer with a Maxwell rheology. The asthenosphere mantle layer is sandwiched between overlying elastic lithosphere and underlying lower mantle, both of which are of high viscosities (Table 1). The shear modulus and densities of the lithosphere and asthenosphere are based on the preliminary reference Earth model (Dziewonski & Anderson 1981), increasing with depth from 2.49 $\times$ 10^{10} to 6.82 $\times$ 10^{10} Pa and 2.6 $\times$ 10^3 to 3.44 $\times$ 10^3 kg m^{-3}, respectively. Other physical parameters in our models are listed in Table 1. We invert for two variables: the thickness of the elastic lithosphere, H_e, and the effective Maxwell decay time of the asthenospheric mantle, T_M. We hold the thickness of the asthenospheric mantle, H_a, fixed at 100 km. We define T_M as $2\eta_a/\mu_a$, where η_a and μ_a, are the viscosity and shear modulus of the asthenospheric mantle, respectively (Table 1).

2.3 Best-fitting viscosity models

We search for viscosity models that minimize the rms misfits between viscoelasic relaxation models and post-seismic observations. Four best-fitting solutions for the post-seismic observations in Types 1, 2 and 3 (Periods a and b), are searched within the variable domain of H_e between 50 and 80 km and T_M between 0.3 and 640 yr.

The best-fitting solution for the Type 1 post-seismic observations is $H_e = 65$ km and $T_M = 0.7$ yr with a rms misfit of 0.25 m (Solution 1, Fig. 3a). It is slightly smaller than the 0.35 m rms misfit that we calculate for the afterslip model of Barrientos & Ward (1990). The observation error for Type 1 data is 0.1 m (Plafker & Savage 1970). We define an acceptable range for T_M values, 0.4 to 1.8 yr, with rms misfits of less than 0.4 m (horizontal error bar in Fig. 3a). The best-fitting solution for the Type 2 post-seismic observations corresponds to $H_e = 67$ km and $T_M = 6$ yr with a rms misfit of 0.67 m (Solution 2, Fig. 3b), similar to the 0.68 m rms misfit for the afterslip model of Barrientos & Ward (1990). The observation error for Type 2 data is 0.34 m (Plafker & Savage 1970). An acceptable range for T_M values defined by rms misfits of less than 0.7 m is between 2.9 and 14 yr (horizontal error bar in Fig. 3b). Figs 4(a) and (b) compare the best-fitting viscoelastic solutions, afterslip model and corresponding observations for Types 1 and 2 data, respectively.

Best-fitting solutions for the Type 3 tidal records yield larger best-fitting T_M values. The best-fitting T_M values are 10 yr for Period a

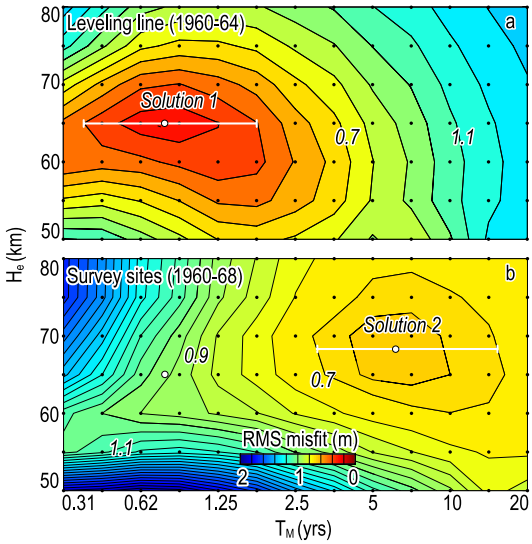

Figure 3. The rms misfits between Type 1 (Panel a) and Type 2 (Panel b) post-seismic observations and volumetric viscoelastic relaxation models. Horizontal axis (T_M) is on a logarithmic scale. Best-fitting solutions are indicated by large black circles: Solution 1 (Panel a, $H_e = 65$ km, $T_M = 0.7$ yr); Solution 2 (Panel b, $H_e = 67$ km, $T_M = 6$ yr). White horizontal error bars indicate T_M ranges that yield acceptable rms misfits.

(Solution 3, Fig. 5a) and 80 yr for Period b (Solution 4, Fig. 5b). We also define acceptable ranges of T_M values, 1.8–40 yr (horizontal error bar in Fig. 5a) and 14–450 yr (horizontal error bar in Fig. 5b), for Periods a and b, respectively. However, Type 3 data do not provide a strong constraint for H_e values (Figs 5a and b). Figs 6(a) and (b) compare the best-fitting solutions with the monthly tidal records for Periods a and b, respectively.

The variations in the best-fitting T_M values can be described by an empirical double exponential function:

$$log[T_M(t)/1\ \mathrm{yr}] = A[1 - e^{(t-to)/\tau}], \quad (1)$$

where t is the time since the 1960 earthquake. Regression analysis yields $A = 1.9$, $t_0 = 2.0$ yr and $\tau = 10.5$ yr (dashed line in Fig. 7). Similar regression processes for the acceptable T_M ranges yield $A = 2.7$, $t_0 = 0.8$ yr and $\tau = 7.8$ yr for the upper bound, and $A = 1.3$, $t_0 = 5.9$ yr and $\tau = 14.8$ yr for the lower bound (within in the grey region in Fig. 7).

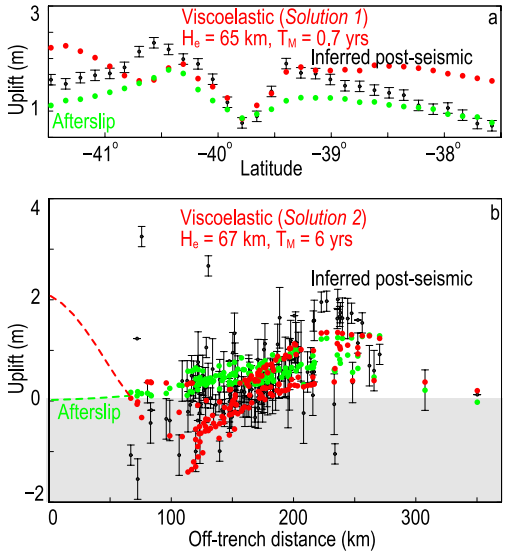

Figure 4. Comparison between observations (black dots and error bars) and best-fitting solutions (red dots): (a) Solution 1 for Type 1 post-seismic deformation and (b) Solution 2 for Type 2 deformation. The error bars indicate observation errors in the geodetic survey (Plafker & Savage 1970). Green dots are the corresponding deformation calculated for the afterslip model of Barrientos & Ward (1990). Red and green dashed lines in (b) show our modelling results near the trench axis for the best-fitting viscoelastic and the afterslip models, respectively.

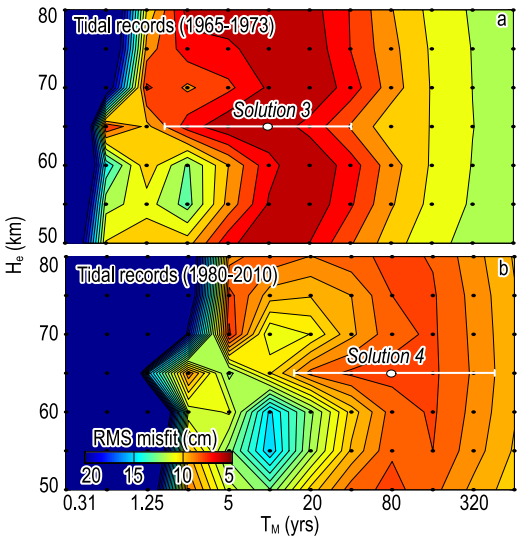

Figure 5. The rms misfits between Type 3 tidal data and viscoelastic models: (a) Solution 3 for 1965–1973 (Period a); (b) Solution 4 for 1980–2010 (Period b). Horizontal axis (T_M) is on a logarithmic scale. The tidal data do not provide a strong constraint for H_e values. Assuming $H_e = 65$ km, we invert for the best-fitting T_M solutions: Solutions 3 (Panel a, $T_M = 10$ yr); Solution 4 (Panel b, $T_M = 80$ yr). White horizontal error bars indicate T_M ranges that yield acceptable rms misfits.

The four best-fitting T_M values correspond to viscosities of 2×10^{18}, 2×10^{19}, 3×10^{19} and 2×10^{20} Pa·s, assuming an asthenospheric shear modulus of $\mu_a = 6.7 \times 10^{10}$ Pa (Table 1). The range of our best-fitting T_M values between 5 and 70 yr for the time period of 1965–1988 (dashed line in Fig. 7) is consistent with the result of Piersanti (1999). The lower bound of our acceptable range of T_M values of 14 yr for the time period of 1993–2005 (grey region in

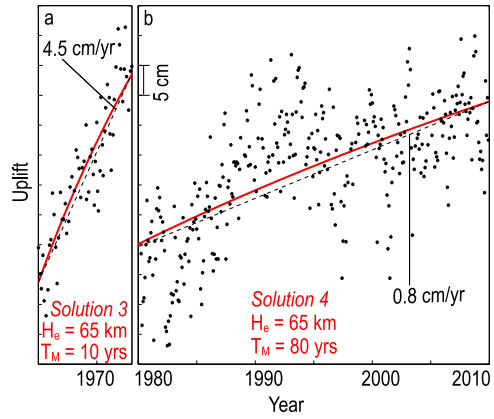

Figure 6. Comparison between Type 3 monthly tidal records (black dots) and best-fitting viscoelastic models (red lines) of (a) Solutions 3 and (b) Solution 4. Dashed black lines indicate linear regression lines with uplift rates of 4.5 cm yr^{-1} (a, in Period a) and 0.8 cm yr^{-1} (b, in Period b).

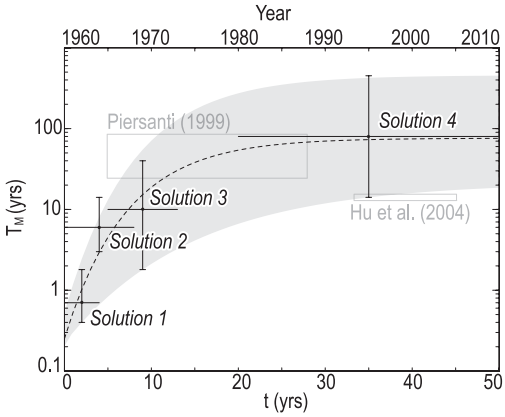

Figure 7. Effective Maxwell decay times, T_M, of Solutions 1–4, and a regression curve in the form of eq. (1) (dashed line). T_M values of Solutions 1–4 and their corresponding acceptable ranges are indicated by dots and error bars for the observation time periods of 1960–1964 (for Type 1 data), 1960–1968 (for Type 2 data), 1965–1973 (for Type 3 Period a data) and 1980–2010 (for Type 3 Period b data), respectively. Grey region is constrained by regression curves for the upper and lower bounds of acceptable T_M values. Grey-line boxes indicate results from Piersanti (1999) and Hu *et al.* (2004).

Fig. 7) is similar to the result based on GPS observations (Hu *et al.* 2004; Fig. 7). The time-dependent increase in the T_M and viscosity values might reflect either a non-linear stress-dependent rheology (Freed & Bürgmann 2004; Freed *et al.* 2006) or a biviscous Burgers rheology of the asthenosphere (Pollitz 2003; Hetland & Hager 2006).

3 POST-1960 STRESS TRANSFER

3.1 Coulomb stress change

For the viscosity structure that best explains the post-seismic deformation, we calculate the Coulomb stress changes on the 1960 and 2010 rupture planes caused by the viscoelastic process. The Coulomb stress change on a receiver fault is defined as:

$$\Delta\mathrm{CFF} = \Delta\tau + \mu\Delta\sigma, \qquad (2)$$

where $\Delta\tau$ is the shear stress change resolved on the receiver fault (positive in the slip direction), $\Delta\sigma$ is the normal stress change on

the receiver fault (positive when the fault is unclamped) and μ is the apparent friction coefficient after accounting for pore pressure, which is assumed to be 0.4 (e.g. King *et al.* 1994). We calculate the stress changes caused by viscoelastic relaxation using the VISCO1D code. We assume the strike, dip and rake angles for the receiver fault of the 2010 earthquake to be 10°, 20° and 90° (Lorito *et al.* 2011), and for the 1960 earthquake to be 7°, 20° and 105° (Barrientos & Ward 1990).

3.2 Post-1960 stress transfer

We first calculate the viscoelastic stress changes on the fault planes of the 1960 and 2010 earthquakes. Viscoelastic deformation and stress changes scale with T_M (Hetland & Hager 2006), so we calculate stress changes at various locations (i.e. locations 1, 2 and 3 in Fig. 8c) as a function of the scaled time, t/T_M, where t is the time since the occurrence of the 1960 earthquake (Fig. 9a). Since the effective T_M increases with time (Fig. 7), we define averaged T_M values, $\tilde{T}_M(t)$, by solving the equation $t/\tilde{T}_M(t) = \int_0^t 1/T_M(t)dt$, where $T_M(t)$ is given by eq. (1). Using $\tilde{T}_M(t)$ instead of T_M, we transform the stress evolution curves in Fig. 9(a) to those in Fig. 9(b). The stress changes are calculated to increase rapidly at first and then level off towards constant values after less than 10 yr. Because the stress evolution depends on temporal T_M functions (eq. 1), we calculate the stress changes for the best-fitting (black line), as well as the upper and lower bound T_M curves (grey region in Fig. 9b).

On the rupture plane of the 1960 earthquake, the region of calculated viscoelastic stress increase is surrounded by areas of negative stress changes on the eastern and western margins (Fig. 8d).

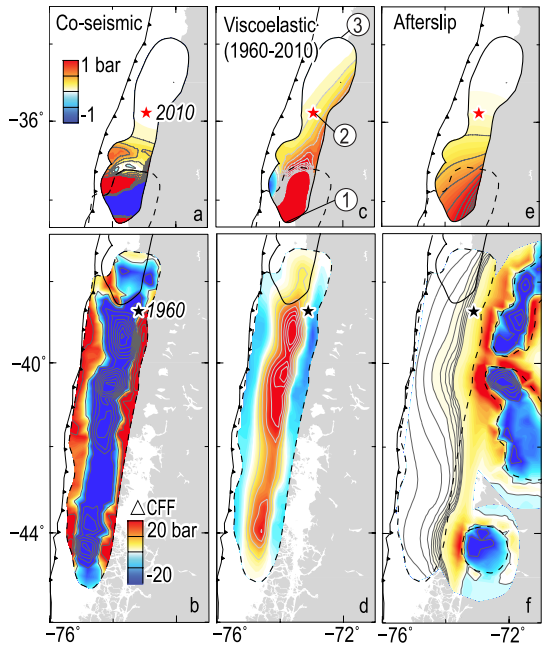

Figure 8. Coulomb stress changes on the rupture plane of the 1960 Valdivia (b, d, f) and 2010 Maule (a, c, e) earthquakes. Red colour indicates positive Coulomb stress change. (a–b) Co-seismic stress changes caused by the 1960 co-seismic slip model of Barrientos & Ward (1990). (c–d) Post-seismic Coulomb stress changes corresponding to our best-fitting volumetric viscoelastic relaxation model with T_M values increasing with time (i.e. dashed curve in Fig. 7). (e–f) Post-seismic Coulomb stress changes due to the afterslip model of Barrientos & Ward (1990) (black dashed contours on the right-hand side of Panel f).

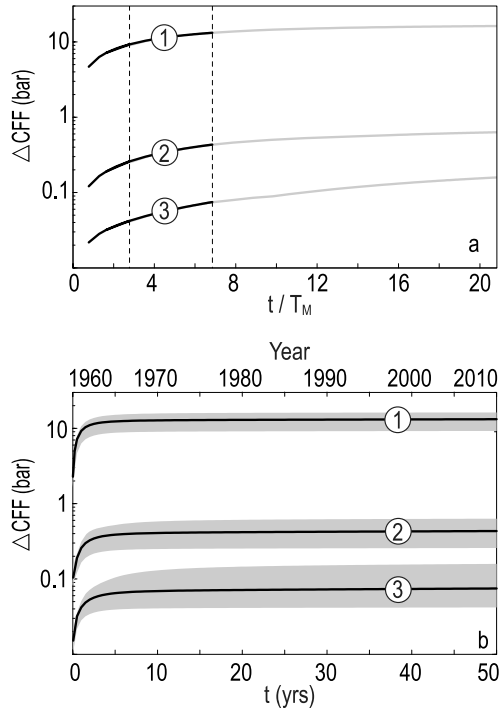

Figure 9. Coulomb stress evolution at locations 1–3 (Fig. 8c) on the rupture plane of the 2010 Maule earthquake. (a) Stress changes at different scaled times, t/T_M. (b) Corresponding stress changes within 50 yr since 1960, assuming that the T_M value increases with time in the form of eq. (1). Black solid curves corresponds to the regression curve for the best-fitting T_M values (dashed curve in Fig. 7), while the grey regions correspond to the lower and upper bound curves of the acceptable T_M ranges (grey region in Fig. 7).

Regions of greater viscoelastic stress increase are located at the depth of 20–50 km, coinciding with the largest co-seismic stress drop of the 1960 earthquake (Fig. 8b). For the best-fitting T_M values and corresponding evolution curve (dashed line in Fig. 7), the maximum stress increase is about 40 bars at the depth of ∼30 km. The maximum stress increase corresponding to the lower and upper bounds of the temporal T_M evolution curves (grey region in Fig. 7) is calculated to be about 30 and 45 bars, respectively. Thus, the viscoelastic stress changes tend to compensate for the co-seismic stress drop on the rupture plane of the 1960 earthquake. Meanwhile, the viscoelastic stress increase corresponding to the best-fitting T_M curve (dashed line in Fig. 7) is calculated to be 13.1 bars at the southern end of the 2010 rupture plane (location 1 in Fig. 8c), gradually decreasing to 0.1 bars at the northern end (location 3). The hypocentre of the 2010 earthquake (location 2) is calculated to have experienced a viscoelastic stress increase of 0.5 bars. We also calculate the stress increases on the 2010 rupture plane for the lower and upper bounds of the temporal T_M evolution curves (grey region in Fig. 7): Location 1 (9.2 and 16.4 bars), location 2 (0.3 and 0.6 bars) and location 3 (0.04 and 0.2 bars; grey regions in Fig. 9b).

We also calculate the stress changes caused by the afterslip model of Barrientos & Ward (1990) using the Coulomb 3.3 software. The afterslip also loads both the 1960 and 2010 rupture planes (Figs 8e and f). On the 1960 rupture plane, the region of greater stress increase due to afterslip is at the depth of about 60 km (Fig. 8f), which is deeper than that for the volumetric viscoelastic relaxation model (Fig. 8d). On the 2010 rupture plane, the afterslip stress increase has a similar along-strike distribution (Fig. 8e) as that

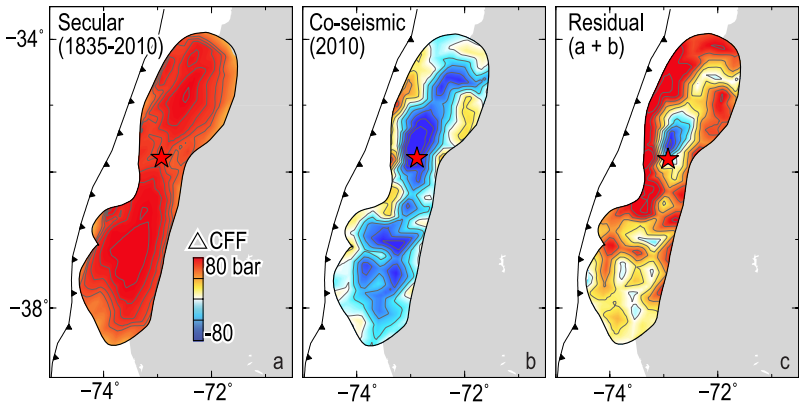

Figure 10. (a) Accumulated Coulomb stress increase within the earthquake cycle of 1835–2010 using a model of variable plate-coupling coefficient inverted from 1996 to 2008 GPS observations (Moreno *et al.* 2010). (b) Co-seismic stress drop of the 2010 Maule earthquake, using the Lorito *et al.* (2011) slip model based on tsunami and geodetic observations. (c) Calculated residual stress after the occurrence of the 2010 earthquake by adding (a) and (b).

of volumetric viscoelastic relaxation (Fig. 8c), but with a smaller maximum stress increase (location 1) of 3.2 bars, compared with 13.1 bars for the viscoelastic relaxation. At the hypocentre of the 2010 earthquake (location 2), the stress increase caused by the afterslip and volumetric viscoelastic relaxation is similar: 0.4 bars (Fig. 8e) and 0.5 bars (Fig. 8c). In comparison, the calculated co-seismic stress increase at the hypocentre of the 2010 earthquake (location 2) caused by the 1960 earthquake is about 0.3 bars (Lin & Stein 2004; Fig. 8a), which is of the same order of magnitude as the post-seismic viscoelastic and afterslip stress increase.

4 DISCUSSION

4.1 Uncertainties in the Type 1 and 2 post-seismic deformation data

Barrientos & Ward (1990) and our study assume that Type 1 and 2 observations contain co-seismic and post-seismic deformation signals. Type 1 and 2 observations may contain other information as well. For example, Linde & Silver (1989) suggested that these observations include pre- and co-seismic signals. Moreno *et al.* (2009) attributed all the deformation to co-seismic slip by using a curved geometry rather than a plane fault. Despite alternative interpretations for the Type 1 and 2 observations, our study shows that the post-seismic deformation, which was previously interpreted as from the afterslip model of Barrientos & Ward (1990), could be equally well explained by the volumetric viscoelastic relaxation of the asthenosphere mantle.

4.2 Viscoelastic relaxation versus afterslip

Our results show that the volumetric viscoelastic relaxation and afterslip could equally explain the geodetic observations in the distance of about 70–370 km away from the Chile trench axis (Fig. 4b). Data that could possibly distinguish the two post-seismic mechanisms include: (1) near-trench seafloor observations (e.g. Newman 2011), (2) long-term geodetic observations or (3) high-density horizontal deformation observations. Our calculations show that the predicted deformation between the volumetric viscoelastic and afterslip models is similar at the distance of more than 70 km from the trench axis, but is different near the Chile trench axis (Fig. 4b). If future seafloor deformation observations are collected, the afterslip and volumetric viscoelastic relaxation models could be distinguished from each other. Another method of distinction is to use long-term geodetic observations: Post-seismic viscoelastic relaxation usually continues within tens of years (Hetland & Hager 2006), while afterslip occurs only within several years after a great earthquake (Helmstetter & Shaw 2009). Finally, Wang *et al.* (2007) argued that the opposing horizontal deformation directions observed at coastal and inland sites of high-density GPS surveys could be explained by post-seismic viscoelastic relaxation, but not afterslip.

4.3 Stress transfer versus tectonic loading

The importance of stress transfer mechanisms to trigger an earthquake must be understood within the framework of the stress evolution in an entire earthquake cycle. The earthquake cycle of the 2010 M8.8 Maule, Chile earthquake could be considered to begin in 1835, when a M8.5 earthquake occurred in the same segment as the 2010 earthquake (Moreno *et al.* 2010; Beck *et al.* 1998). During its earthquake cycle, the 2010 rupture plane is loaded by plate convergence due to the coupling between the subducting Nazca Plate and the overriding South America Plate. We estimate this secular tectonic stress using a GPS-inverted plate-coupling model with variable coupling coefficient (Moreno *et al.* 2010), assuming a plate convergence rate of 6.6 cm yr^{-1} (Angermann *et al.* 1999). Our calculations show that the tectonic stress increase and the 2010 co-seismic stress drop are of the similar 'two-patch' spatial patterns (Figs 10a and b). The 2010 earthquake is calculated to have released a similar magnitude of stress as the stress accumulated by the secular tectonic loading in 1835–2010.

The above similarities also suggest that the 2010 rupture plane was close to failure before the occurrence of the 2010 Maule earthquake. Therefore, a relatively small amount of additional stress increase, such as that due to co- and post-seismic processes caused by the nearby 1960 earthquake, could contribute to the triggering of the 2010 earthquake.

We also estimate the residual stress after the occurrence of the 2010 earthquake by adding the 1835–2010 tectonic and 2010 co-seismic stresses. The post-1835 tectonic stress accumulated on the slip patch to the north of the 2010 hypocentre seems to be fully released, while the southern patch is still associated with a certain

amount of residual stresses (Fig. 10c), similar to the interpretations of Moreno *et al.* (2010) based on slip deficit calculation.

5 CONCLUSIONS

Our investigation of the post-seismic deformation of the 1960 *M*9.5 Valdivia, Chile earthquake and the associated stress transfer yields the following results:

1. Three types of post-1960 geodetic observations during four time periods could be explained by a volumetric viscoelastic relaxation model equally well as the previous afterslip models. The observations in four sequential time periods could be explained by a consistent elastic lithosphere thickness of about 65 km, but require a significant increase in the effective Maxwell decay times of the asthenospheric mantle.
2. The inverted effective Maxwell decay times of the asthenosphere mantle are 0.7, 6, 10 and 80 yr to best explain the observations during the time periods of 1960–1964, 1960–1968, 1965–1973 and 1980–2010, respectively.
3. The rupture plane of the 2010 Maule, Chile earthquake is calculated to have experienced stress increase of 0.1–13.1 bars due to post-1960 viscoelastic relaxation, in comparison to 0.1–3.2 bars due to afterslip. These post-1960 stress increases might have contributed to the triggering of the 2010 earthquake.

ACKNOWLEDGEMENTS

We are grateful to Andrés Tassara of the University of Concepcion for help accessing the PSMSL tidal gauge data in Chile. We thank Fred Pollitz of USGS for providing the VISCO1D code and technical consultation on using the code. This study also benefitted from discussion with Mark Behn, Ikudo Wada, Nathaniel Miller, Matt Wei, Shane McGary and the Marine Tectonics Group of WHOI, Andrew Freed of Purdue University, Sergio Barrientos of the University of Chile and Ross Stein of USGS. This work was supported by a MIT/WHOI Joint Program Student Fellowship and a Graduate Student Fellowship from the WHOI Deep Ocean Exploration Institute (MD), as well as NSF Grant OCE-1141785 and a Deerbrook Foundation Award (JL).

REFERENCES

Angermann, D., Klotz, J. & Reigber, C., 1999. Space-geodetic estimation of the Nazca-South America Euler vector, *Earth planet. Sci. Lett.,* **171,** 329–334.

Barrientos, S.E. & Ward, S.N., 1990. The 1960 Chile earthquake: inversion for slip distribution from surface deformation, *Geophys. J. Int.,* **103,** 589–598.

Barrientos, S.E., Plafker, G. & Lorca, E., 1992. Postseismic coastal uplift in southern Chile, *Geophys. Res. Lett.,* **19,** 701–704.

Beck, S., Barrientos, S., Kausel, E. & Reyes, M., 1998. Source characteristics of historic earthquakes along the central Chile subduction zone, *J. S. Am. Earth Sci.,* **11,** 115–129.

Dziewonski, A.M. & Anderson, D.L., 1981. Preliminary reference Earth model, *Phys. Earth Plan. Int.,* **25,** 297–356.

Freed, A.M., 2005. Earthquake triggering by static, dynamic, and postseismic stress transfer, *Annu. Rev. Earth Plan. Sci.,* **33,** 335–367.

Freed, A.M. & Bürgmann, R., 2004. Evidence of power-law flow in the Mojave desert mantle, *Nature,* **430,** 548–551.

Freed, A.M., Bürgmann, R., Calais, E. & Freymueller, J., 2006. Stress-dependent power-law flow in the upper mantle following the 2002 Denali, Alaska, earthquake, *Earth planet. Sci. Lett.,* **252,** 481–489.

Helmstetter, A. & Shaw, B.E., 2009. Afterslip and aftershocks in the rate-and-state friction law, *J. geophys. Res.,* **114,** doi:10.1029/2007JB005077.

Hetland, E.A. & Hager, B.H., 2006. The effects of rheological layering on post-seismic deformation, *Geophys. J. Int.,* **166,** 277–292.

Hu, Y., Wang, K., He, J., Klotz, J. & Khazaradze, G., 2004. Three-dimensional viscoelastic finite element model for postseismic deformation of the great 1960 Chile earthquake, *J. geophys. Res.,* **109,** doi:10.1029/2004JB003163.

King, G.C.P., Stein, R.S. & Lin, J., 1994. Static stress changes and the triggering of earthquakes, *Bull. seism. Soc. Am.,* **84,** 935–953.

Linde, A.T. & Silver, P.G., 1989. Elevation changes and the great 1960 Chilean earthquake:support for aseismic slip, *Geophys. Res. Lett.,* **16,** 1305–1308.

Lin, J. & Stein, R.S., 2004. Stress triggering in thrust and subduction earthquakes and stress interaction between the southern San Andreas and nearby thrust and strike-slip faults, *J. geophys. Res.,* **109,** doi:10.1029/2003JB002607.

Lorito, S., Romano, F., Atzori, S., Tong, X., Avallone, A., McCloskey, J., Cocco, M., Boschi, E. & Piatanesi, A., 2011. Limited overlap between the seismic gap and coseismic slip of the great 2010 Chile earthquake, *Nat. Geosci.,* **4,** 173–177.

Moreno, M.S., Bolte, J., Klotz, J. & Melnick, D., 2009. Impact of megathrust geometry on inversion of coseismic slip from geodetic data: application to the 1960 Chile earthquake, *Geophys. Res. Lett.,* **36,** doi:10.1029/2009GL039276.

Moreno, M., Rosenau, M. & Oncken, O., 2010. 2010 Maule earthquake slip correlates with pre-seismic locking of Andean subduction zone, *Nature,* **467,** 198–202.

Newman, A.V., 2011. Hidden depths, *Nature,* **474,** 441–443.

Piersanti, A., 1999. Postseismic deformation in Chile: constraints on the asthenospheric viscosity, *Geophys. Res. Lett.,* **26,** 3157–3160.

Plafker, G. & Savage, J.C., 1970. Mechanism of the Chilean Earthquakes of May 21 and 22, 1960, *Geol. Soc. Am. Bull.,* **81,** 1001–1030.

Pollitz, F.F., 1992. Postseismic relaxation theory on the spherical earth, *Bull. seism. Soc. Am.,* **82,** 422–453.

Pollitz, F.F., 2003. Transient rheology of the uppermost mantle beneath the Mojave Desert, California, *Earth planet. Sci. Lett.,* **215,** 89–104.

Tichelaar, B.W. & Ruff, L.J., 1991. Seismic coupling along the Chilean Subduction Zone, *J. geophys. Res.,* **96,** 11997–12022.

Toda, S., Stein, R.S., Richards-Dinger, K. & Bozkurt, S., 2005. Forecasting the evolution of seismicity in southern California: animations built on earthquake stress transfer, *J. geophys. Res.,* **110,** doi:10.1029/2004JB003415.

Wang, K., 2007. Elastic and viscoelastic models of crustal deformation in subduction earthquake cycles, in *The Seismogenic Zone of Subduction Thrust Faults,* eds Dixon, T. & Moore, J.C., Columbia Univ. Press

Wang, K., Hu, Y. & He, J., 2012. Deformation cycles of subduction earthquakes in a viscoelastic Earth, *Nature,* **484,** 327–332.

Wang, K., Hu, Y., Bevis, M., Kendrick, E., Smalley, R., Vargas, R.B. & Lauría, E., 2007. Crustal motion in the zone of the 1960 Chile earthquake: Detangling earthquake-cycle deformation and forearc-sliver translation, *Geochem. Geophys. Geosyst.,* **8,** doi:10.1029/2007GC001721.

APPENDIX A: MODEL SENSITIVITY OF VISCOELASTIC DEFORMATION

The calculated post-seismic viscoelastic deformation depends on two key variables: the thickness of elastic lithosphere, H_e, and the effective Maxwell decay time of the asthenosphere mantle, T_M. We assume a 100-km-thick asthenosphere mantle.

1. Types 1 and 2 observations

With decreasing H_e values, the calculated Type 1 deformation becomes more positive (Fig. A1a). Meanwhile, the distance of the region of the calculated maximum uplift from the trench axis decreases for Type 2 data (Fig. A1b). For both Type 1 (Fig. A2a) and Type 2 (Fig. A2b) data, a reduction in T_M leads to more positive calculated deformation.

2. Type 3 observations

The calculated post-1960 deformation at the Puerto Montt station increases exponentially with time (Fig. A3). For both Period a (1965–1973, Fig. A3a) and Period b (1980–2010, Fig. A3b) data, all the H_e values in the range of 50–80 km explain the observations well, assuming a constant T_M. Thus, Type 3 observations do not provide a strong constraint for H_e values. For both Period a (Fig. A3c) and Period b (Fig. A3d), a reduction in T_M leads to an increase in the calculated rate of deformation, assuming a constant H_e.

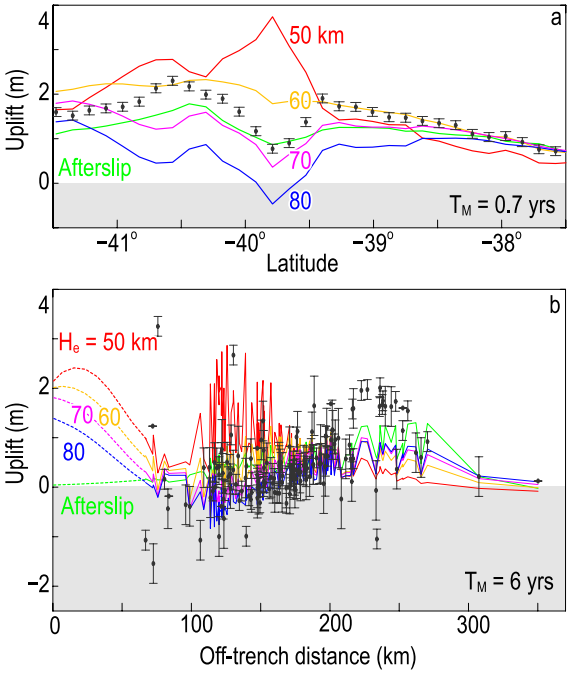

Figure A1. Calculated deformation for (a) Type 1 and (b) Type 2 observations assuming different lithospheric thickness: H_e = 50 km (red), 60 km (orange), 70 km (magenta), 80 km (blue). Green curves correspond to the afterslip model (Barrientos & Ward 1990). Black dots with error bars indicate the corresponding post-1960 land-level changes. Viscoelastic models assume constant T_M values of 0.7 yr (Solution 1) in (a) and 6 yr (Solution 2) in (b).

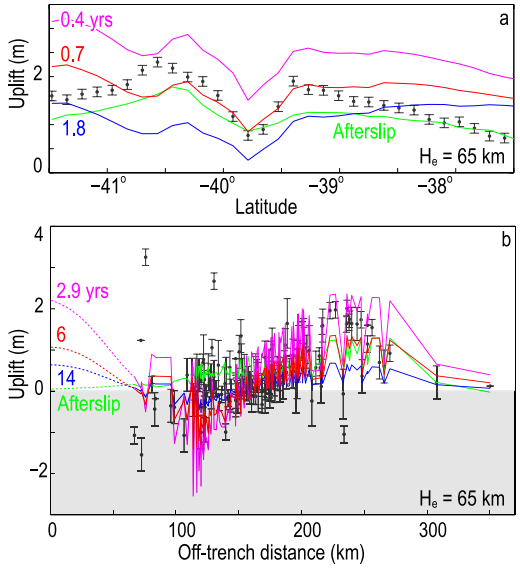

Figure A2. Calculated Type 1 and 2 deformation for viscoelastic models with different T_M values: best-fitting T_M (red), as well as lower (blue) and upper (purple) bounds of the acceptable T_M ranges. Viscoelastic models assume a constant H_e value of 65 km. Green curves correspond to the afterslip model (Barrientos & Ward 1990). Black dots with error bars indicate the corresponding post-1960 land-level changes. (a) For Type 1 observations. (b) For Type 2 observations.

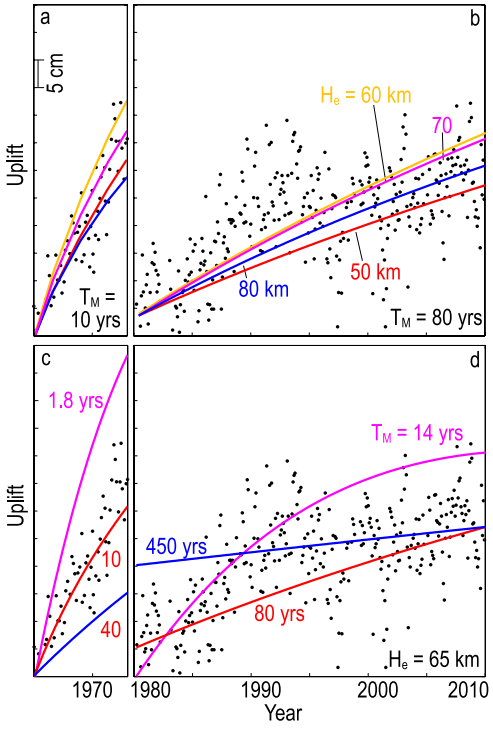

Figure A3. Calculated deformation at the tidal station Puerto Montt for two time intervals: (a, c) Period a of 1965–1973 and (b, d) Period b of 1980–2010. Black dots are the observed monthly time-series. Post-seismic viscoelastic models with different H_e and T_M values are shown by different colours. (a–b) Modelling results for different H_e values, 50, 60, 70 and 80 km, assuming T_M to be 10 yr in (a) and 80 yr in (b). (c–d) Modelling results for different T_M values: best-fitting T_M (red), as well as lower (blue) and upper (purple) bounds of the acceptable T_M ranges, assuming H_e = 65 km.